PAPER

Fluidic origami cellular structure with asymmetric quasi-zero stiffness for low-frequency vibration isolation

IOP Publishing Smart Materials and Structures
Smart Mater. Struct. **28** (2019) 065006 (15pp) https://doi.org/10.1088/1361-665X/ab143c

Fluidic origami cellular structure with asymmetric quasi-zero stiffness for low-frequency vibration isolation

Sahand Sadeghi and Suyi Li

Department of Mechanical Engineering, Clemson University, Clemson, SC 29634, United States of America

E-mail: ssadegh@clemson.edu

Received 30 November 2018, revised 12 March 2019
Accepted for publication 28 March 2019
Published 1 May 2019

Abstract

This study investigates a unique asymmetric quasi-zero stiffness (QZS) property from the pressurized fluidic origami cellular structure, and examines the feasibility and efficiency of using this nonlinear property for low-frequency vibration isolation. This QZS property of fluidic origami stems from the nonlinear geometric relationships between folding and internal volume change, and it can be programmed by tailoring the constituent Miura-Ori crease design. Different fluidic origami cellular structure designs are introduced and examined to obtain a guideline for achieving QZS property. A proof-of-concept prototype is fabricated to experimentally validate the feasibility of acquiring QZS. Moreover, a comprehensive dynamic analysis is conducted based on numerical simulation and harmonic balance method approximation. The results suggest that the QZS property of fluidic origami can successfully isolate base excitation at low frequencies. In particular, this study carefully examines the effects of an inherent asymmetry in the force–displacement curve of pressurized fluidic origami. It is found that such asymmetry could significantly increase the transmissibility index with certain combinations of excitation amplitude and frequency, and it could also induce a drift response. Outcome of this research can lay the foundation for new origami-inspired multi-functional metamaterials and meta-structures with embedded dynamic functionalities. Moreover, the investigations into the asymmetry in force–displacement relationship provide valuable insights for many other QZS structures with similar properties.

Keywords: fluidic origami, quasi-zero stiffness, base excitation isolation, nonlinear dynamics

(Some figures may appear in colour only in the online journal)

1. Introduction

The ancient Japanese art of Origami is essentially a technique of developing topologically intricate three-dimensional shapes by folding. Its beauty and simplicity have fostered a surge of interest from the science, mathematics, architecture, and engineering communities. For example, molecular biologists used origami method to fold single-stranded DNA molecules into predetermined shapes, which can be used to form complex self-assembled nanostructures (Andersen *et al* 2009, Dietz *et al* 2009, Ke *et al* 2009, Shih and Lin 2010). Plant biologists examined the deployment of seed capsules, leaves, and flowers based on origami folding principles (Kaino *et al* 2000, Street 2002, Harrington *et al* 2011). Mathematicians developed computational tools that can design the appropriate crease patterns for achieving desired shape reconfigurations by folding (Tachi 2010a, 2010b, Waitukaitis and van Hecke 2016). Engineers also investigated the feasibility of utilizing origami for a wide variety of applications. For example, it is possible to fold flat sheet into stiff and lightweight structures such as sandwich panels with fold cores (Schenk and Guest 2013), folded plate shell structures (Yoshimura 1951), and cellular solids (Kamrava *et al* 2017). Moreover, it can be advantageous to leverage the

kinematics (aka. shape reconfiguration) of origami folding to advance the deployable aerospace structures (Miura 1985, Zirbel *et al* 2013, Schenk *et al* 2014), self-folding robots (Felton *et al* 2014, Peraza-Hernandez *et al* 2014, Na *et al* 2015), medical stents (Kuribayashi *et al* 2006), and flexible electronics (Song *et al* 2014). Recently, there has been a paradigm shift from harnessing the kinematics of origami to utilizing the mechanics of folding for engineering purposes (Li *et al* 2018). As a result, we are witnessing the rapid emergence of origami mechanical metamaterials. These metamaterials are typically made of multiple stacked origami sheets with carefully designed crease patterns (Tachi 2011, Schenk and Guest 2013, Cheung *et al* 2014, Eidini 2016), and the intricate relationships between folding and constituent sheet deformations can impart the origami metamaterials with unique and even unorthodox mechanical properties. For example, it has been demonstrated that origami-based metamaterials and meta-structures can exhibit negative and flipping Poisson's ratio (Schenk and Guest 2013, Eidini and Paulino 2015, Yasuda and Yang 2015, Sadeghi and Li 2019, Fang *et al* 2016), self-locking and discrete stiffness jumps (Fang *et al* 2018, Fang *et al* 2016, Kamrava *et al* 2017), and elastic multi-stability (Daynes *et al* 2014, Hanna *et al* 2014, Silverberg *et al* 2015, Waitukaitis and van Hecke 2016, Fang *et al* 2017, Sengupta and Li 2018). In addition, the stacked origami topology features naturally embedded tubular channels, which can be pressurized to generate adaptive functions. This is the idea behind the so-called *pressurized fluidic origami cellular structure* (referred simply as 'fluidic origami' hereafter), which arises from combining the physical principles behind the plant nastic movements and the design variety of the origami art (figure 1). By utilizing the relation between folding motion and the enclosed internal fluid volume, fluidic origami is able to exhibit many interesting characteristics. For example it has been studied for its capabilities to achieve shape transformation, stiffness control, and recoverable collapse (Li and Wang 2015, Li *et al* 2016).

Despite these remarkable developments, current state-of-the-art mainly focuses on the kinematics and quasi-static applications of origami folding. However, origami-inspired structures and materials could also show interesting dynamic characteristics under excitations due to the richness of folding geometry. Nevertheless, studying the dynamic characteristics of origami-based structures is still a nascent field and there are only a few researches conducted in this area hitherto. Yasuda *et al* (2016) studied the nonlinear elastic wave propagation in a multiple degree-of-freedom origami metamaterial consisting of Tachi–Miura polyhedron (TMP) cells. They investigated the feasibility of harnessing the geometry-induced nonlinearity of the TMP-based tubular metamaterials for tunable vibration and impact mitigation. Fang *et al* (2017) studied the dynamic characteristics of a bi-stable stacked Miura-Ori (SMO) structure and investigated its application in vibration isolation at certain frequencies. Ishida *et al* proposed a cylindrical truss structure, inspired by the Kresling folding pattern, for vibration isolation and investigated its performance numerically and experimentally (Ishida *et al* 2017a, 2017b, Inamoto and Ishida 2018). This vibration isolation

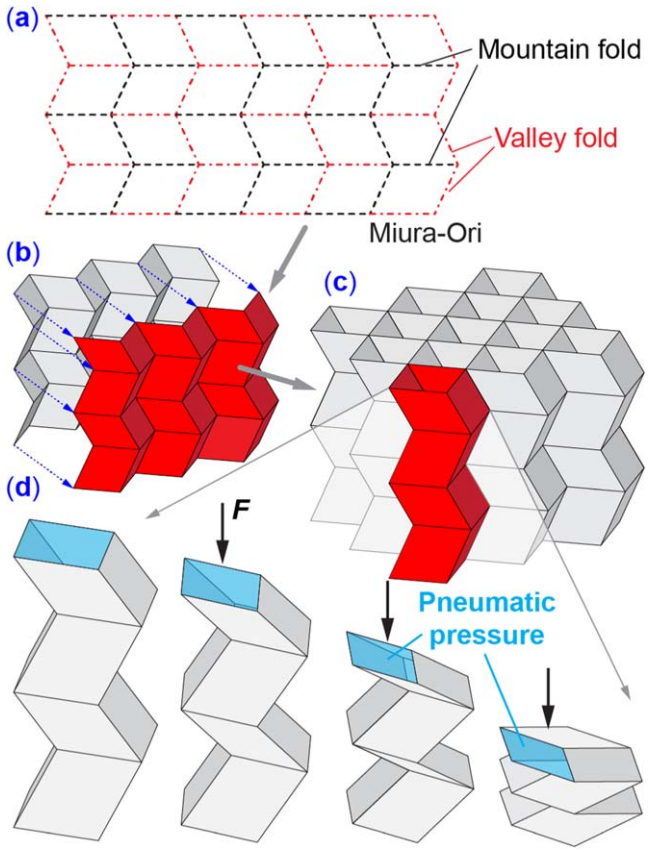

Figure 1. The concept of pressurized fluidic origami cellular structure. (a) Crease pattern of the underlying Miura-Ori. (b) Folded Miura-Ori sheets with compatible designs can be stacked and connected to form a space-filling cellular architecture shown in (c). (d) The fluidic origami features naturally embedded tubular channels, which can be pressurized pneumatically. Such pressurization induces the desired quasi-zero stiffness property.

function stems from a quasi-zero stiffness (QZS) property obtained by combining the bi-stability of the Kresling pattern and a linear spring. Other than these studies, there are no other literatures on the dynamics induced by origami folding. Therefore, the foremost vision of this research is to expand our knowledge and understand on how to harness the folding-induced mechanical properties to foster a new family of multi-functional origami structures and material systems with dynamic applications. To this end, we introduced a unique QZS characteristics from the pressurized fluidic origami and investigated the feasibility of using this mechanical property for low-frequency vibration isolation (Sadeghi and Li 2017). Unlike the cylindrical truss structure studied by Ishida *et al* the QZS properties of the fluidic origami does not arise from mechanical springs but rather stems from interaction between internal pressure and folding. This provides a unique mechanism for developing an adaptive QZS vibration isolator.

Exploiting quasi-zero-stiffness has been an important topic in low-frequency vibration isolation for decades. For a passive vibration isolator consisting of a mass (m) supported by a linear spring (k), vibration isolation occurs in frequencies over $\sqrt{2k/m}$ (Thomson and Dahleh 1997). Consequently, one would prefer a smaller stiffness (k) to increase the usable

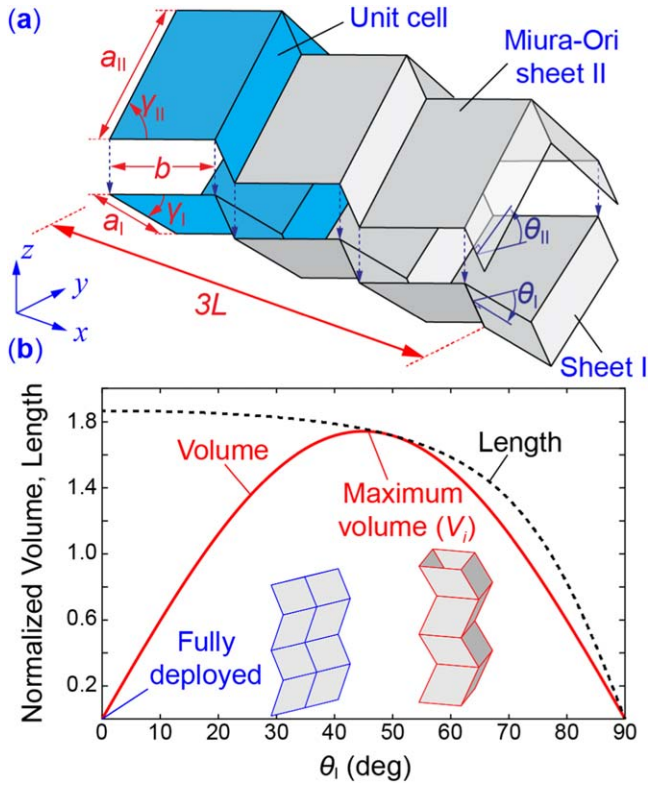

Figure 2. The design and kinematics of fluidic origami. (a) The geometry of a tubular channel in fluidic origami, showing the definition of a, b, γ, and θ of the two Miura-Ori sheets. The unit cell is highlighted, and in this plot, the tubular channel has three unit cells (aka. $N = 3$). (b) The strongly nonlinear relationships between geometric quantities and folding angle. In this plot, $a_{II} = a_I = b$, and $\gamma = 70°$. The normalized volume $\hat{V} = V/Na_I^3$ and normalized length $\hat{L} = L/Na_I$.

frequency bandwidth; however, this would result in a very small static load carrying capacity. Implementing nonlinear springs with QZS property can be an advantageous solution for this problem. Using the QZS property, the dynamic stiffness of the system would be close to or ideally zero at the equilibrium position, while the static stiffness remains large. Therefore, the system can minimize the vibrations transmission at very low frequencies without sacrificing the static load carrying capacity. Recently, researchers have proposed different types of QZS isolation devices that have been utilized in various engineering fields, e.g. vibration isolation of precision instruments, vibration resonance test of aircraft, suspensions and seats of vehicles and even gravitational wave detection (Hao and Cao 2015). Several methods of creating and harnessing the QZS property have been proposed, such as combining vertical and oblique linear springs (Carrella *et al* 2007, Carrella 2008, Kovacic *et al* 2008), incorporating load-bearing elastic elements of positive stiffness with devices of negative stiffness (Alabuzhev *et al* 1989), using structural buckling (Lee *et al* 2007, Fulcher *et al* 2014), and electromagnetic negative stiffness elements (Zhou and Liu 2010). Moreover, it is worth noting that a lot of valuable resources on the dynamic analysis of QZS isolation systems can be found in the literature. From analyzing the transmissibility characteristics of a third-order Duffing dynamic system (Carrella *et al* 2009a, 2012) to studying frequency characteristics of complex intrinsic behaviors, such as primary, sub/super harmonic and chaotic motions that possibly occur in the QZS systems (Hao and Cao 2015). In the authors' previous publication, it was shown that QZS property could arise from combining the pressure-induced stiffness and the nonlinear geometric relationships between folding and internal volume (Sadeghi and Li 2017). The QZS property is naturally embedded in the structure without the need of any additional springs like in other devices; furthermore, it is feasible to obtain a wide range of appropriate Miura-Ori designs to reach QZS.

The previous study by the authors, however, mainly focused on the design principles of obtaining the QZS property in fluidic origami without any experimental validation, and a comprehensive investigation on its dynamic responses from a low-frequency base excitation is lacking. Such dynamics study is indeed crucial for understanding its performance potentials and limitations as a vibration isolator. Moreover, the reaction force–displacement relationship of the fluidic origami exhibits a strong *asymmetry*. The influence of such asymmetry on the base excitation isolation can be significant at certain input frequencies and magnitudes. There are a few relevant studies dealing with asymmetries rising from equilibrium offset or a constant external force based on systems with otherwise symmetric force–displacement curves (Kovacic *et al* 2008, 2009, Abolfathi 2012, Huang *et al* 2014, Abbasi *et al* 2016). The asymmetry in fluidic origami, on the other hand, is unique in that it is an inherent property stemming from the folding kinematics, so understanding its influence is crucial for the dynamic analysis. Therefore, the objective of this study is to conduct a thorough analytical and experimental investigation on obtaining QZS property in fluidic origami, and then elucidate the influences of asymmetry in its QZS property for low-frequency vibration isolation. Results of this study can lay the foundation for the emergence of a new category of multi-functional, origami-based metamaterials and metastructures with adaptive dynamic functionalities.

The remaining sections of this paper are organized as follows. Section 2 recapitulates the nonlinear geometrical relationships between origami folding and the desired QZS characteristics. A design criterion for obtaining the QZS property is also presented. Section 3 discusses the experimental verification of the existence of QZS property in a proof-of-concept fluidic origami prototype. Section 4 details the dynamic analysis of utilizing the investigated asymmetric QZS property for base excitation isolation. The behavior of the fluidic origami is analyzed numerically, and harmonic balance method (HBM) is also used to provide deeper insights into the fundamental dynamic characteristics. Section 5 concludes this paper with summary and discussion.

2. Folding kinematics and the origin of QZS property

In this section, we briefly discuss the physical principles underpinning the QZS property in fluidic origami, which lays the foundation for the further dynamic investigations. The concept of fluidic origami is based on the idea that connecting Miura-Ori folded sheets along their zig-zag crease lines can create a space-filling cellular topology with naturally embedded tubular features (figure 1) (Li and Wang 2015). Miura-Ori is a periodic tessellation, thus one can concentrate on studying the unit cell shown in figure 2(a) as a representative of the whole structure. Three geometric parameters, which remain unchanged regardless of folding, determine the design of Miura-Ori folding pattern. They are the length of two adjacent crease lines (a, b), and the sector angle (γ) between these two lines. Miura-Ori folding pattern is rigid foldable, therefore the facet material can be assumed rigid and the creases can be treated as ideal hinges. With these assumptions, the folding motion of Miura-Ori has one degree-of-freedom that can be described by the dihedral folding angle (θ) defined between the x–y reference plane and the constituent facets (figure 2(a)). To ensure kinematic compatibility so that Miura-Ori sheets do not separate from each other during folding, one needs to apply two geometric constraints: $b_{\mathrm{II}} = b_{\mathrm{I}} = b$, and $a_{\mathrm{I}} \cos\gamma_{\mathrm{I}} = a_{\mathrm{II}} \cos\gamma_{\mathrm{II}}$, where the sub index I and II represents to the two Miura-Ori sheets in a unit cell (Schenk and Guest 2013). In this way, the folding angles of the two Miura-Ori sheets are directly related so that $\cos\theta_{\mathrm{I}} \tan\gamma_{\mathrm{I}} = \cos\theta_{\mathrm{II}} \tan\gamma_{\mathrm{II}}$, and the rigid folding of the fluidic origami retains one degree of freedom.

In this study, we choose the folding angle θ_{I} as the independent variable to describe the folding motion so that the unit cell length can be calculated as follows (Li and Wang 2015):

$$L = \frac{2b\cos\theta_{\mathrm{I}}\tan\gamma_{\mathrm{I}}}{\sqrt{1+\cos^2\theta_{\mathrm{I}}\tan^2\gamma_{\mathrm{I}}}}. \tag{1}$$

Based on these governing geometric relationships, the enclosed volume of the unit cell can be derived as follows

$$V = 2a_{\mathrm{I}}^2 b\sin^2\gamma_{\mathrm{I}}\cos\theta_{\mathrm{I}}\left(\sqrt{\frac{\tan^2\gamma_{\mathrm{II}}}{\tan^2\gamma_{\mathrm{I}}} - \cos^2\theta_{\mathrm{I}}} + \sin\theta_{\mathrm{I}}\right). \tag{2}$$

Equations (1), (2) describe the kinematic connections between the external geometries and internal volume change of fluidic origami. Based on these relationships, one can predict that the fluidic origami will fold to a configuration with maximum enclosed volume when it is subject to internal pressure (Li *et al* 2016). This is due to the entropy increase from inner energy reduction by volume expansion (Gramüller *et al* 2014). Pressurization also imparts nonlinear stiffness to the structure (aka. pressure-induced stiffness (Li *et al* 2016)). If the fluidic origami structure is subject to external mechanical loads along the x direction (defined in figure 2(a)), the reaction force due to internal pressure can be calculated as follows based on virtual work principle:

$$F_L = -P\frac{\mathrm{d}V}{\mathrm{d}L} = -P\frac{\mathrm{d}V}{\mathrm{d}\theta_{\mathrm{I}}}\left(\frac{\mathrm{d}L}{\mathrm{d}\theta_{\mathrm{I}}}\right)^{-1}, \tag{3}$$

where $\mathrm{d}L$ is the change in origami length along the external force exertion direction. The pressure-induced stiffness can be defined as the variation of the reaction force with respect to the infinitesimal deformation so that (Li *et al* 2016):

$$k_L = \frac{\mathrm{d}F}{\mathrm{d}L}. \tag{4}$$

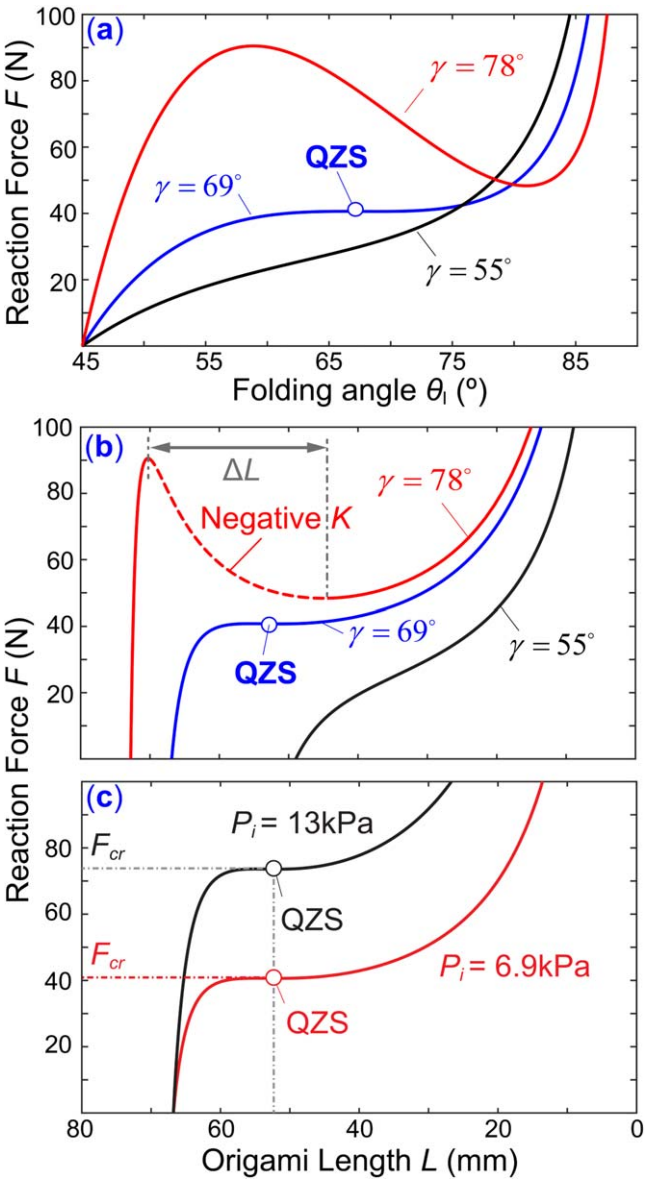

Figure 3. Pressure-induced stiffness of the fluidic origami unit cell based on PV = const. (a) The reaction force-folding angle relationship, showing the influence of sector angle (γ). (b) The influence of γ angle on the force-deformation relationship. (c) Reaction force-deformation curves based on different initial pressures (P_i). In all of these figures: $a = b = 38$ mm.

By observing the force–displacement relationship in equation (3) or the corresponding pressure-induced stiffness, we can investigate the feasibility of obtaining QZS in fluidic origami. To this end, we consider the following scenario of pressurization. The fluidic origami is pressurized with an ideal gas at an initial pressure (P_i) until it folds and settles at the configuration with maximum possible internal volume (V_i). Then the structure is sealed so that the total amount of pressurized gas inside is kept constant. After this, if the fluidic origami deforms via folding due to an external force, its internal pressure (P) and enclosed volume (V) will change accordingly. The ideal gas law states that $PV = nRT$, where n is the amount of substance of gas (in moles), R is the universal gas constant, and T is the absolute temperature of the gas. We assume that the change in internal volume due to folding occurs slowly so the gas temperature (T) is constant. Moreover, n is constant due to the sealing of fluidic origami. Therefore, we can conclude that:

$$PV = P_i V_i = \text{const}, \tag{5}$$

and the reaction force equation (3) can be updated as follows:

$$F_L = -\frac{P_i V_i}{V}\frac{\mathrm{d}V}{\mathrm{d}\theta_\mathrm{I}}\left(\frac{\mathrm{d}L}{\mathrm{d}\theta_\mathrm{I}}\right)^{-1}. \tag{6}$$

Based on equation (6), it can be seen that the reaction force and pressure-induced stiffness of the fluidic origami are functions of the internal volume (V) and the length (L) of the unit cell. Figure 2(b) shows that these two geometric variables are strongly nonlinear functions of the folding angle (θ_I). Therefore, we can also expect the pressure-induced reaction force and stiffness are strongly nonlinear with respect to the overall folding deformation. It is possible to prescribe the behavior of the force–displacement curve and obtain the desired QZS characteristic for vibration isolation by choosing the appropriate design for the Miura-Ori pattern. In the following subsections, two different design cases are presented, the first case is identical stacked Miura-Ori sheets (ISMO) and the second one is non-identical stacked Miura-Ori sheets (NISMO).

2.1. Case 1: identical stacked Miura-Ori sheets (ISMO)

With two identical Miura-Ori sheets, the previously discussed relationships can be simplified because $\gamma_\mathrm{II} = \gamma_\mathrm{I} = \gamma$ and $a_\mathrm{II} = a_\mathrm{I} = a$. figures 3(a), (b) shows the force-deformation curves of different ISMO tubes with 2 unit cells based on the same crease lengths ($a = b = 38$ mm) but different γ angles. Initial pressure (P_i) is the same at 6.9 kPa. It can be seen that when the sector angle γ is less than 69°, the reaction force increases monotonically with deformation, implying a nonlinear positive stiffness. When $\gamma > 69°$, the reaction force curve has a segment of negative stiffness. The critical, quasi-zero-stiffness can be achieved when the sector angle equals to 69°. At this particular sector angle, the length of the negative stiffness segment in the reaction force curve converges to zero. In other words, the tangent stiffness of the fluidic origami is positive throughout its deformation range except for the QZS configuration, where the tangent stiffness equals to zero.

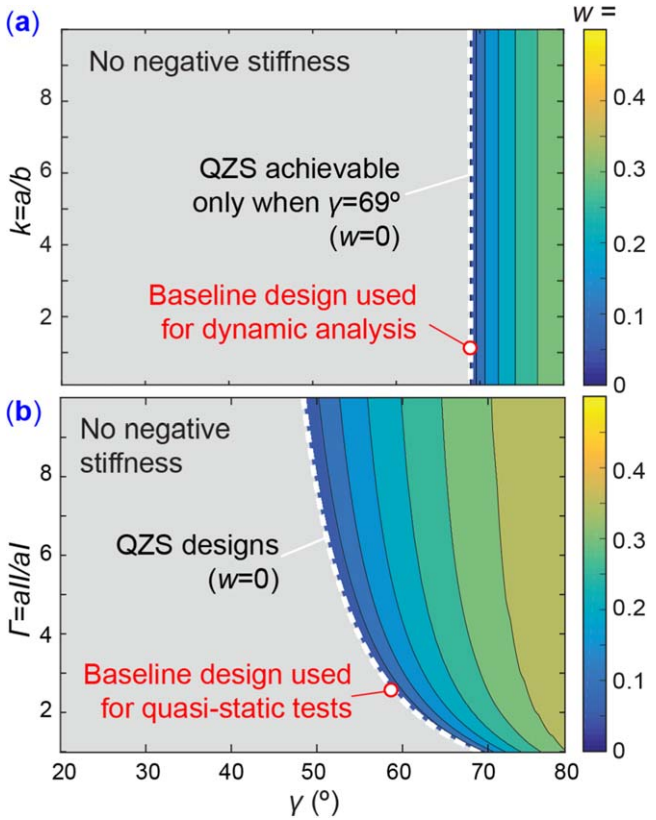

Figure 4. Parametric studies for obtaining QZS properties. (a) The relationship between the deformation range with negative stiffness and ISMO design parameters. Grey region represents designs that would not generate any negative stiffness. (b) The relation between the deformation range with negative stiffness and NISMO design parameters. In both cases, Miura-Ori designs that can give QZS property are highlighted. The designs used in the following quasi-static experiment (section 3) and dynamic analysis (section 4) are highlighted.

There are several interesting properties from the ISMO fluidic origami of $\gamma = 69°$. First of all, the QZS characteristic is achievable regardless of the initial pressure (P_i). Secondly, the magnitude of reaction force at the QZS point (F_{cr}) is linearly proportional to the magnitude of initial pressure. Finally, the deformation at the QZS point is only a function of origami geometry and does not depend on the initial pressure (figure 3(c)). In section 3, we will detail the benefits of these properties in vibration isolation. In order to find a comprehensive design criterion to obtain the QZS characteristics, we introduce a non-dimensional parameter w as follows:

$$w = \frac{\Delta l}{Na}, \tag{7}$$

where Δl is the deformation range with negative stiffness in the reaction force–displacement curve (figure 3(b)), and N is the number of unit cells in a tubular channel. Δl needs to be zero in order to achieve the QZS property in the force–displacement curve. Figure 4(a) illustrates the result of the parametric study on the correlation between w and the

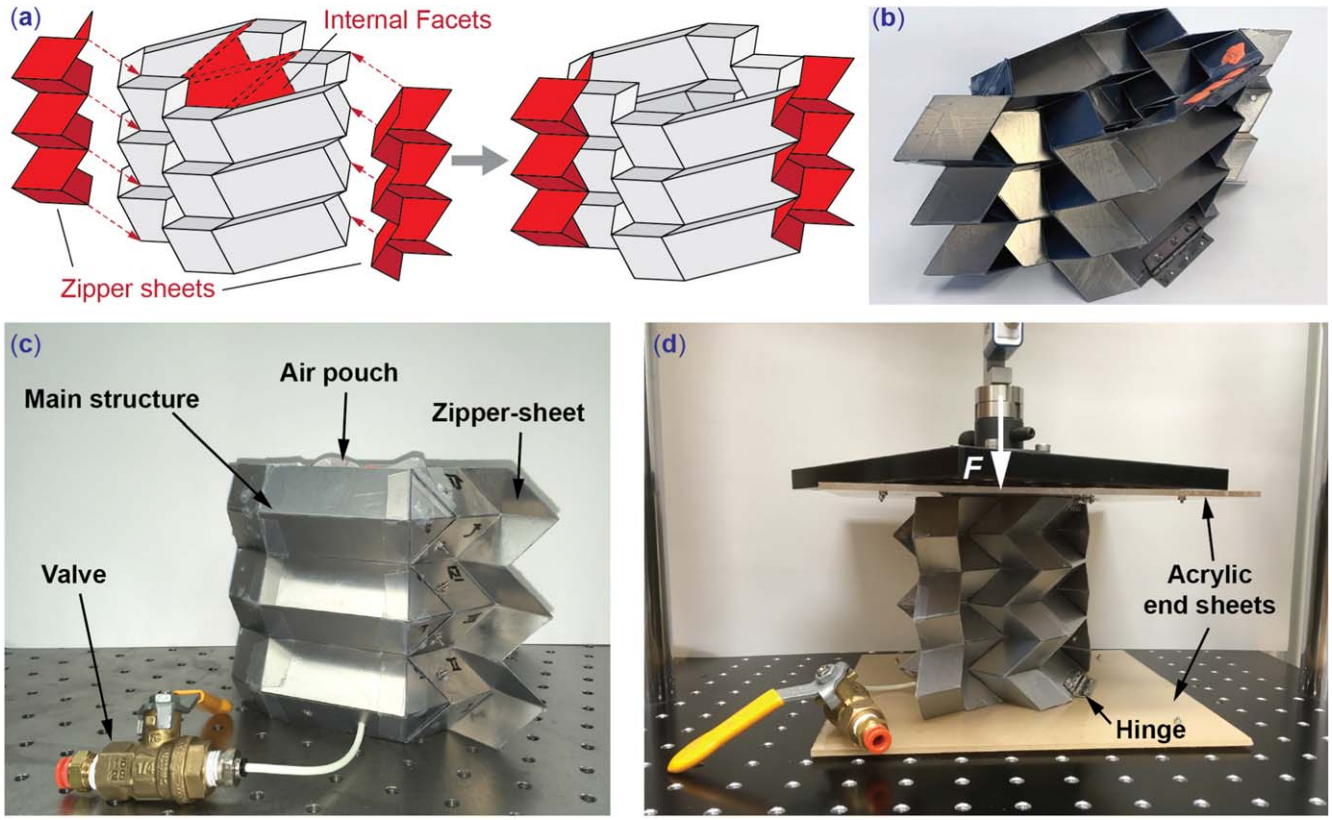

Figure 5. Proof-of-concept experimental tests. (a) Schematic drawing showing the design and assembly of the fluidic origami prototype. The zipper-sheets and internal facets are highlighted. (b) Finished prototype made from waterjet cut steel sheets and adhesive plastic films. (c) In this figure, the fluidic origami prototype has been pressurized through a custom-made air pouch to its maximum internal volume configuration. Note that the end valve has been closed and disconnected from the pressure supply to ensure a constant PV according to the governing equation (6). (d) The experimental set-up for the quasi-static test.

Miura-Ori design. It can be seen that for identical Miura-Ori sheets, w is independent of the creases length ratio k $(=a/b)$ and is only a function of sector angle (γ). Based on the aforementioned governing equations and results presented in the figure 4(a), we can conclude that QZS is reachable only when $\gamma = 69^\circ$ regardless of the crease lengths (a and b).

2.2. Case 2: NISMO sheets

To study the design criteria for obtaining QZS when the fluidic origami consists of two different Miura-Ori sheets, we introduce a new non-dimensional parameter (Γ) to quantify the design difference between the two sheets:

$$\Gamma = \frac{a_{\mathrm{II}}}{a_{\mathrm{I}}}. \tag{8}$$

We can follow the same procedure as in the ISMO case to obtain the design criteria for obtaining QZS property in the NISMO case. The results of the parametric study in this case is presented in figure 4(b). In the NISMO case, the designs that can provide QZS depend on both the sector angles and the ratio between crease line lengths. Therefore, the parametric study results in figure 4 can provide the design guidelines to achieve QZS and further dynamic analyses discussed in the section 4.

3. Proof-of-concept prototype and the quasi-static test

To validate the feasibility of achieving the desired QZS property in fluidic origami, we fabricate and test a proof-of-concept prototype. This prototype is designed to possess the characteristics of an origami structure with rigid facets and hinge-like creases. To this end, facets are first waterjet cut individually from a 0.25 mm thin stainless-steel sheet. Then 0.13 mm thin adhesive-back plastic films (ultra high molecular weight Polyethylene) are used to connect the facets together into a complete origami sheet with hinge-like soft creases. This origami prototype resembles a NISMO structure with four connected tubular channels, each consisting three unit-cells (figure 5(a)). Design parameters used in this prototype are summarized in table 1. The fluidic origami prototype is also equipped with two 'zipper sheets' to constrain the overall deformation to rigid-folding only. These zipper-sheets have the same designs as the smaller Miura-Ori sheet I used in the main structure, but they are rotated about the lengthwise x-axis (figure 5(a)). Because of this rotation, the zipper-sheet can drastically increase the eigen-stiffness of undesired deformations (e.g. bending and squeezing) without hindering the rigid-folding deformation (Filipov *et al* 2015).

Furthermore, we remove the internal facets in the fluidic origami prototype so that the four initially separated channels

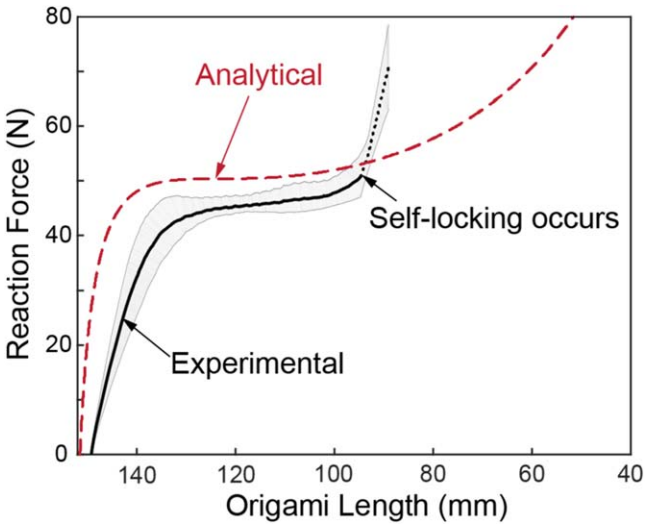

Figure 6. The force–displacement relationships. The dashed curve represents the analytical result and the solid and dotted curve shows the averaged experimental result. The shaded grey region represents the standard deviation of the measurements.

Table 1. Design parameters used in the proof-of-concept prototype.

a_{I}	b	a_{II}	γ_{I}	γ_{II}
30 mm	30 mm	$2.5a_{\mathrm{I}}$	59°	78°

are combined into one (figures 5(a), (b)); this makes it much easier to apply a uniform internal pressure. Removing the internal facets, however, does not change the governing relationship between internal pressure and reaction force as defined in equation (6), because it does not alter the kinematic relationships between rigid-folding, total volume, and overall length of the fluidic origami. A custom-made cubic-shaped air pouch is inserted to the fluidic origami to provide internal pressurization. The pouch is made of 0.1 mm thin low-density polyethylene film. The mass of the completed fluidic origami prototype is about 200 grams.

The main structure is then connected to two 2.77 mm thick clear cast acrylic end sheets using 0.635 mm thick piano hinges to provide the required contact surface for the quasi-static compression test. It is worth noting that this hinge only anchor one origami facet to the end sheet (figure 5(d)), and other facets in contact with the end sheets are free to move. The compressive force–displacement curve of the pressurized fluidic origami structure is tested on a tensile test machine (ADMET eXpert 5601 with a 250lbf load cell, 3 mm min^{-1} displacement rate) (figure 5(d)). The structure is pressurized with initial pressure of 1.38 kPa until it reaches its maximum volume (figure 5(c)). During testing, the pressurized air is constrained inside the air pouch by closing the connected on/off valve (figure 5(c)). Five sets of measurements are performed; and figure 6 depicts the averaged force–displacement curve, the corresponding standard deviation, and the analytical prediction based on equation (6). The quasi-static test on the fluidic origami structure exhibits a good repeatability among the five sets of measurements, and the standard deviation is about 3% of the average value in the QZS region.

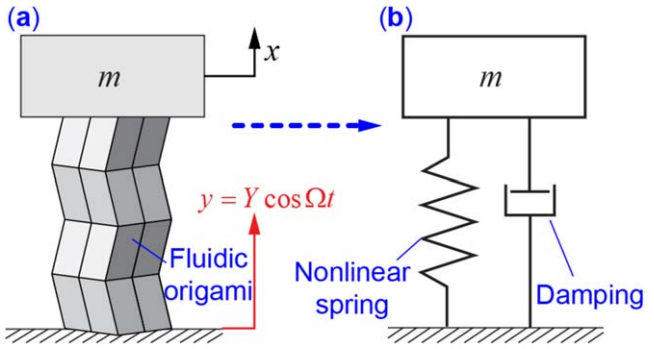

Figure 7. Setup of the dynamic analysis. (a) Schematic diagram of using fluidic origami for base vibration isolation. (b) The equivalent discrete system.

Test results reported in figure 6 match the analytical prediction well, especially, the pressure-induced QZS behavior is evident. There are some discrepancies between test results and analytical prediction, which are probably caused by two reasons: one is the imperfect contact between air pouch and inner surface of the facets, which is not considered in the model. The other cause is non-rigid folding deformations (e.g. bending and squeezing) that are observed especially at higher internal pressures (Li and Wang 2015, Li *et al* 2016). In addition, one should notice a sudden jump in reaction force before the fluidic origami is fully folded. This is because the screws used to connect the zipper-sheets to the main structure come into contact with the facets so further folding is prevented. However, right before such a self-locking occurs, we can clearly observe a gradual increase in reaction force and effective stiffness beyond a QZS region, which stems from the physics underlying the pressurized fluidic origami. Therefore, despite the abovementioned discrepancies, the presented results validate the existence of the pressure-induced QZS in fluidic origami.

4. Dynamic analysis of fluidic origami with QZS properties

In this section, we examine the effectiveness of utilizing the fluidic origami for low-frequency base excitation isolation. To avoid unnecessary complexities, here we use the design parameters obtained in the ISMO case study, that is $a_{\mathrm{II}} = a_{\mathrm{I}} = a$, $b = a$, and $\gamma = 69°$. However, the physical principles and design insights obtained in this case study can be applied to any other fluidic origami designs that can exhibit QZS property. Figure 7 illustrates the system setup for vibration isolation, where the fluidic origami is assumed massless and a lumped mass ($m = 1$ kg) is attached at the top. In this way, one can describe the origami structure as a combination of a nonlinear spring and a damping element between the lumped mass and base. It is worth highlighting that utilizing the QZS property for vibration isolation requires that the static equilibrium of the mass-spring-damper system

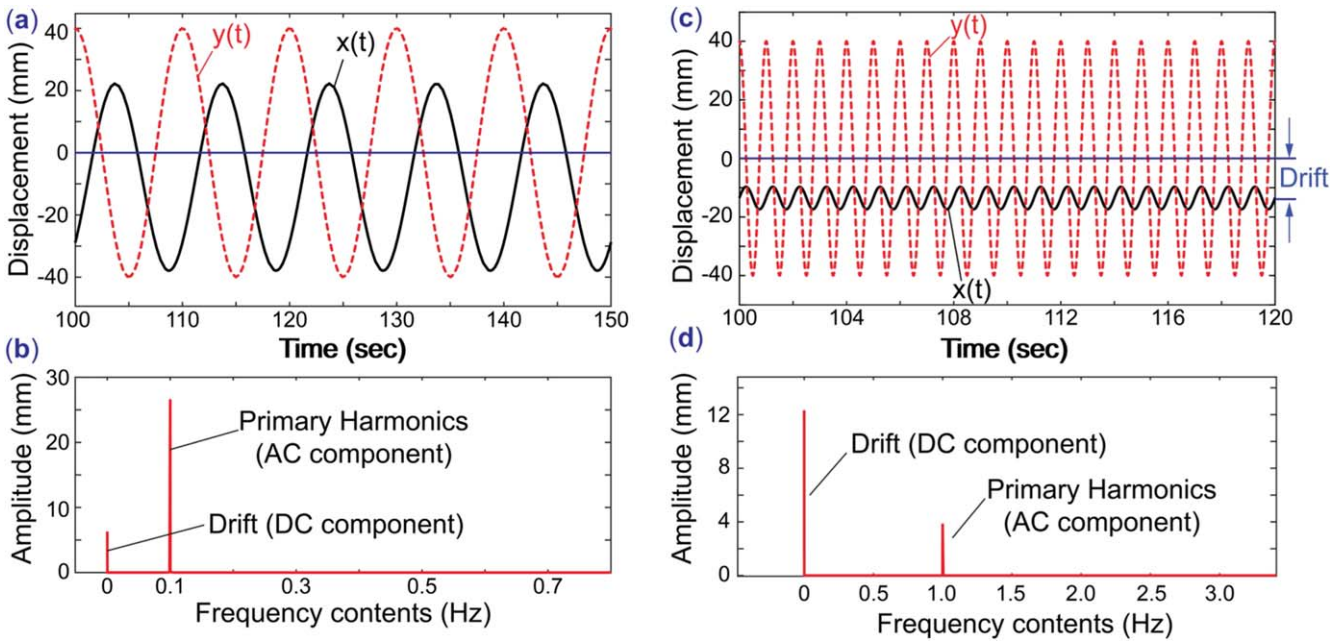

Figure 8. Numerical simulation of the fluidic origami isolator based on actual force–displacement curve according to equation (6). (a), (b) Sample steady-state time response with $\Omega = 0.1$ Hz, $Y = a$ and the corresponding FFT result. (c), (d) Another sample response with different input ($\Omega = 1$ Hz, $Y = a$).

shown in figure 7 occurs at the QZS configuration. That is, the weight of the lumped mass should be equal to the reaction force at the QZS point ($mg = F_{cr}$). To achieve this, we can use the unique property of pressurized fluidic origami that the magnitude of the reaction force at the QZS configuration is linearly proportional to the magnitude of the initial pressure (figure 3(c)). Therefore, the initial pressure can be adjusted according to the following equation:

$$P_i = mg\left[-\left(\frac{V_i}{V}\right)\frac{\mathrm{d}V}{\mathrm{d}L}\right]^{-1}\Bigg|_{\mathrm{QZS}}. \tag{9}$$

We can then write the governing dynamic equation of motion as:

$$\ddot{u} + 2\zeta\dot{u} + F(u) = \Omega^2 Y\cos\Omega t, \tag{10}$$

where, $u = x - y$ is the relative displacement between the lumped mass and base. $F(u)$ is the reaction force of the fluidic origami. ζ is the damping coefficient, which is assumed be to 0.3 for this study based on a relevant study on the dynamics of bistable origami structure (Fang *et al* 2017). It is worth noting that this damping coefficient is not experimentally measured, and it can change if the fluidic origami is fabricated in a different way, but we do not expect a change in damping can fundamentally alter the vibration isolation behavior of fluidic origami. Ω is the excitation frequency, and Y is the base excitation amplitude. The reaction force (F), which exhibits the desired QZS characteristics, is determined based on the fluidic origami constitutive relationship in equation (6) and appropriate initial pressure according to equation (9). To characterize the performance of the base excitation isolation, we introduce a transmissibility index (TR), defined as the ratio of the root mean squares of mass and base displacements $x(t)$ and $y(t)$, respectively:

$$\mathrm{TR} = \frac{\mathrm{rms}(x(t))}{\mathrm{rms}(y(t))}. \tag{11}$$

The governing equation of motion (10) based on the actual force–displacement curve (equation (6)) is solved numerically using MATLAB 'ode23s' solver. The steady-state time response (examples shown in figure 8) can be used to calculate the TR.

Beside numerical simulation, another common method for examining the QZS vibration isolators is to use *odd* order polynomials to approximate the reaction force–displacement curve around the QZS point, so that the established dynamic analysis methods like HBM can be used. For example, a third-order polynomial approximation can be applied to QZS structures and effectively turns the overall system into a classical Duffing oscillator (Carrella *et al* 2007, Kovacic *et al* 2008, Carrella *et al* 2009a, 2009b, 2012). Zhou *et al* (2015) also used a cubic polynomial by truncating the Taylor series expansion about the equilibrium to examine a cam-roller-spring QZS isolator. Some other studies even used fifth odd order polynomials (Neild and Wagg 2011, Shaw *et al* 2013).

Nonetheless, these odd order polynomial fittings are fundamentally similar in that they produce *symmetric* force displacement curves with respect to the zero origin. That is, $f(x) = -f(-x)$, where x is an arbitrary displacement from the QZS point and $f(x)$ is the force–displacement relationship. However, the force displacement curve of the fluidic origami shown in figure 3 is strongly asymmetric. To understand how such asymmetry influences the dynamic response and performance of base excitation isolation, we apply both symmetric (section 4.1) and asymmetric (section 4.2) polynomial fitting,

and compare the corresponding HBM results to the dynamic response based on the actual force–displacement curve.

4.1. Dynamic analysis based on symmetric polynomial fitting

A simple, symmetric cubic fitting assumes the reaction force $F(u) \simeq \alpha u^3$, where the cubic stiffness coefficient α can be found via the least square method (figure 7(a)). The governing equation of motion (10) can be updated accordingly to:

$$\ddot{u} + 2\zeta\dot{u} + \alpha u^3 = \Omega^2 Y \cos \Omega t. \tag{12}$$

This essentially represents a Duffing oscillator with a zero linear stiffness term. Assuming a fluidic origami structure consisting of two internally connected unit cells ($N = 2$) and an initial pressure of $P = 13.8$ KPa, the cubic stiffness coefficient turns out to be $\alpha = 81\,020$ N m^{-3}.

The steady state solution of equation (12) can be approximated by HBM, which is a powerful method for analyzing the steady-state behavior of strongly nonlinear dynamic systems (Hamdan and Burton 1993, Nayfeh 1993, Carrella *et al* 2009a). According to HBM, the solution of equation (12) can be approximated as:

$$u(t) = U_1 \cos \Omega t + U_2 \sin \Omega t. \tag{13}$$

Substituting the assumed $u(t)$ into the simplified dynamic equation (12) and discarding higher order harmonic terms give the following nonlinear polynomial equations:

$$\begin{cases} -\Omega^2 U_1 + 2\Omega\zeta U_2 + \frac{3}{4}\alpha {U_1}^3 + \frac{3}{4}\alpha U_1 {U_2}^2 - \Omega^2 Y = 0, \\ -\Omega^2 U_2 - 2\Omega\zeta U_1 + \frac{3}{4}\alpha {U_2}^3 + \frac{3}{4}\alpha U_2 {U_1}^2 = 0, \end{cases} \tag{14}$$

which can be solved numerically to obtain the two unknown coefficients (U_1, U_2). Once these two coefficients are determined, equation (12) can be updated to provide the approximate solution for the relative displacement $u(t)$ and then the TR index. Figures 9(b), (c) show the TR obtained by numerical simulation and HBM corresponding to two different base excitation amplitudes: $Y = 0.125Na$ and $Y = 0.75Na$, where a is the crease line length, and N is the number of cells. For the small excitation amplitude, HBM results based on a cubic fitting agree well with the numerical simulation; however, there are significant discrepancies at the higher excitation amplitude. Such discrepancy in TR magnitude at higher excitation amplitude is also shown in figure 9(d), which depicts the comparison between cubic fitting prediction and numerical simulation for a wide range of excitation amplitudes with a constant frequency ($\Omega = 0.1$ Hz). Therefore, the HBM results based on symmetric polynomial fitting cannot accurately predict the qualitative behavior of the base isolation behavior, especially at higher excitation amplitudes.

Besides the discrepancies in transmissibility predictions at higher excitation amplitude, the symmetric cubic fitting also fails to predict the emergence of a drift or zero-frequency 'DC component' observed in the numerical simulation based on the actual-force displacement curve (figures 8(b), (d)). Such a drift or DC component is especially evident at a higher

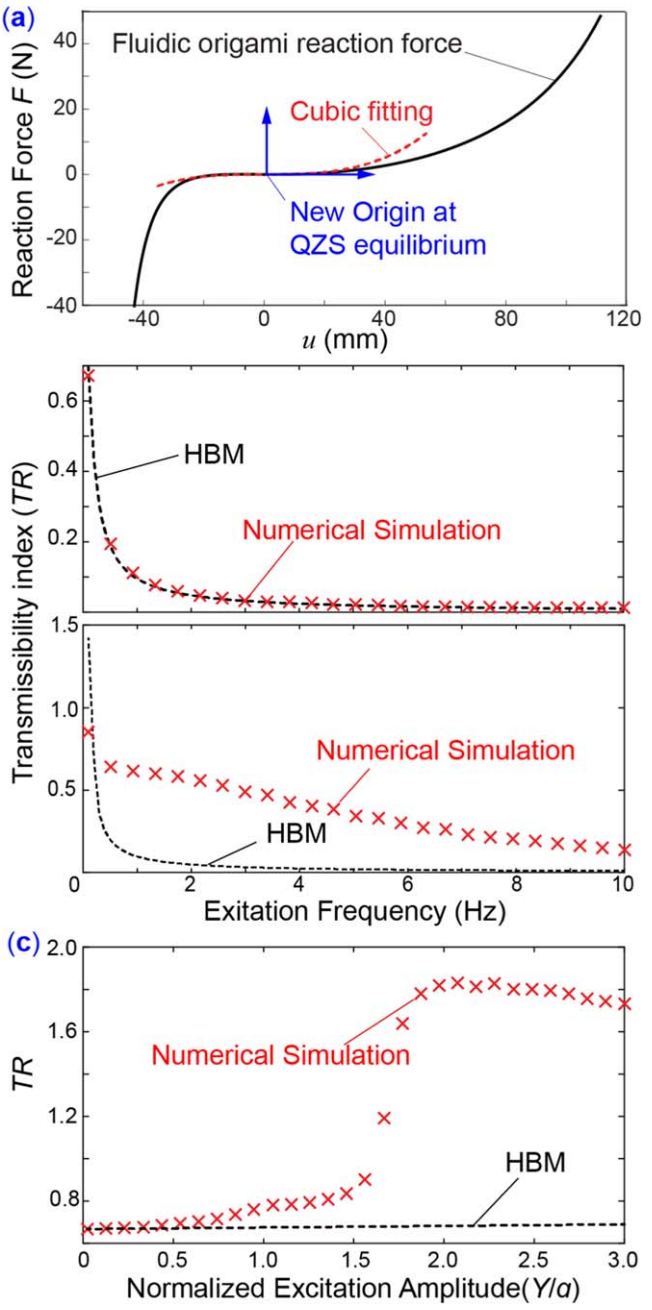

Figure 9. Dynamic analysis based on symmetric cubic polynomial fitting. (a) The setup of cubic polynomial fitting. (b), (c) Relationships between TR and excitation frequencies at $Y = 0.125Na$ and $0.75Na$, respectively. (d) The relationship between TR and excitation amplitudes ($\Omega = 0.1$ Hz).

frequency (figure 8(b)) so that the lumped mass moves to another position rather than the static equilibrium and oscillates around that point. Indeed, it can be proven that for any dynamic system described by a second order differential equation of the form:

$$\ddot{u} + c\dot{u} + f(u) = F \cos(\Omega t), \tag{15}$$

where the reaction force $f(u)$ is a summation of odd-order polynomials exhibiting a symmetric behavior around the

origin:

$$f(u) = \alpha_{m_1} u^{m_1} + \alpha_{m_2} u^{m_2} + ... + \alpha_{m_n} u^{m_n}, \tag{16}$$

and $m_i (i = 1, 2, ..., n)$ are odd and positive integers, the system cannot exhibit any drift or zero frequency response. To prove by contradiction, we assume the solution of equation (15) includes a constant drift term U_0 so that:

$$u = U_0 + U_1 \cos \Omega t + U_2 \sin \Omega t. \tag{17}$$

Applying HBM and collecting zero-frequency components produces the following equation:

$$\begin{aligned}
&U_0 \sum_{k=0}^{k_{f_1}=\frac{m_1-1}{2}} \sum_{l=0}^{l_{f_1}=\frac{m_1-(2k+1)}{2}} {U_0}^{2k} (\alpha_{l_1} {U_1}^{m_1-(2k+1)-2l} {U_2}^{2l}) + \ ... \\
&U_0 \sum_{k=0}^{k_{f_2}=\frac{m_2-1}{2}} \sum_{l=0}^{l_{f_2}=\frac{m_2-(2k+1)}{2}} {U_0}^{2k} (\alpha_{l_1} {U_1}^{m_2-(2k+1)-2l} {U_2}^{2l}) + \ ... \\
&U_0 \sum_{k=0}^{k_{f_n}=\frac{m_n-1}{2}} \sum_{l=0}^{l_{f_n}=\frac{m_n-(2k+1)}{2}} {U_0}^{2k} (\alpha_{l_1} {U_1}^{m_n-(2k+1)-2l} {U_2}^{2l}) = 0
\end{aligned} \tag{18}$$

It is obvious that $2k$, $m_i - (2k + 1) - 2l$, and $2l$ are all positive even integers. Since U_0, U_1, and U_2 are real values, equation (18) only has two possible solutions:

$$\begin{cases} U_0 = 0, \\ U_0 = U_1 = U_2 = 0, \end{cases} \tag{19}$$

and only the first solution is non-trivial. Therefore, we can conclude that for any dynamic system described by equation (15), which has a symmetric reaction force–displacement, it cannot produce any drift or zero-frequency response as $U_0 = 0$.

Therefore, it can be concluded that a symmetric approximation of the force displacement curve could not fully capture the dynamic behaviors of the fluidic origami. Our results imply that the asymmetry of the fluidic origami force–displacement relationship is crucial in that: (1) it could significantly increase the TR at higher excitation amplitudes and (2) it could induce a drift response. To validate these observations, we add *even*-order polynomials to our fitting to introduce an asymmetry around the QZS point, and the corresponding predictions are discussed in the following subsection.

4.2. Dynamic analysis based on asymmetric polynomial fitting

It should be noted that the reaction-force displacement of the fluidic origami is a complex nonlinear function; therefore, it is extremely hard to replicate its exact behavior through polynomial fitting. Obviously, a higher order polynomial fitting can better replicate the force displacement curve of the fluidic origami. Figure 10(a) shows the comparison between some polynomial fittings, which indicates that one needs to consider a ninth-order polynomial curve to obtain a *quantitatively* accurate prediction. However, including a ninth-order polynomials in HBM makes the study extremely arduous and unreasonable. Alternatively, we can concentrate on *qualitatively* revealing the effects of asymmetry on the overall

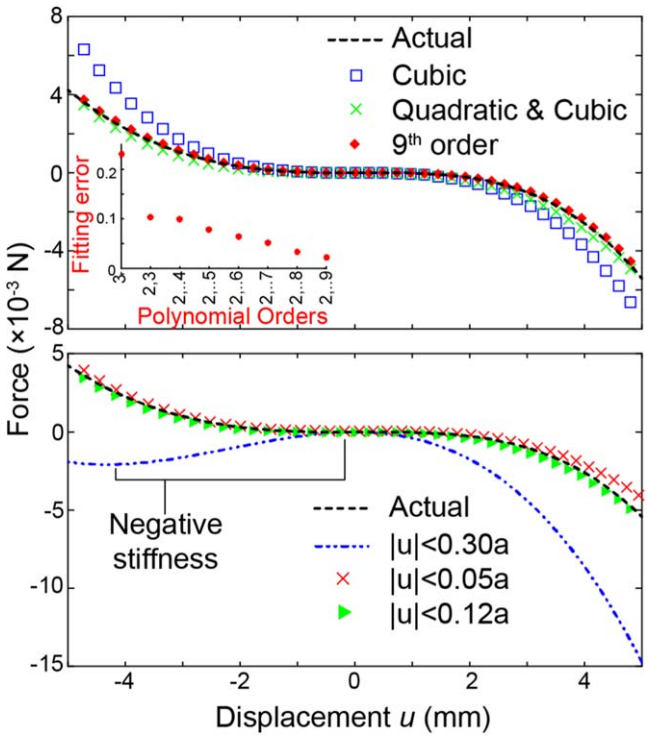

Figure 10. Fitting with quadratic and cubit polynomial terms. (a) Comparison between some polynomial fittings with different orders performed for range $|u| < 0.12a$. The insert plot shows the corresponding magnitude of fitting error ($= \mathrm{rms}(u_{actual} - u_{fit})/\mathrm{rms}(u_{actual})$). (b) Actual force–displacement curve and the comparison of three different fitting results based on cubic and quadratic polynomials with different ranges of fitting.

system dynamics. For this reason, we use the simplest fitting that can preserve the asymmetric behavior of the force–displacement curve, that is, a combination of second and third order polynomials. It is worth noting that there should not be a linear term in the fitting in order to satisfy the zero stiffness at the origin. With these considerations, force–displacement function can be approximated as:

$$F(u) = \alpha_2 u^2 + \alpha_3 u^3, \tag{20}$$

where the quadratic and cubic stiffness term α_2 and α_3 are approximated by the least square method. Estimating the values of these two stiffness terms are not trivial. Figure 8(b) shows the actual force–displacement curve according to equation (6) along with three different fitting results. These fittings all include cubic and quadratic terms as in equation (20), but differ in the displacement range where the least square method is applied. It can be clearly seen that if the range is too big, the fitting is not able to replicate the QZS property of the actual force displacement-curve, that is, the sign of stiffness changes to negative near origin. On the other hand, if the range is too small, the fitting deviates significantly from the actual force displacement curve. Therefore, one needs to use the maximum displacement range for fitting as long as the QZS property is qualitatively preserved at the equilibrium point ($|u| < 0.12a$ in this case), which results in: $\alpha_2 = 333\,004\ \mathrm{N\,m^{-2}}$, $\alpha_3 = 51\,260\ \mathrm{N\,m^{-3}}$.

By incorporating the quadratic and cubic fitting, the equation of motion (10) can be updated to:

$$\ddot{u} + 2\zeta\dot{u} + \alpha_2 u^2 + \alpha_3 u^3 = \Omega^2 Y \cos \Omega t. \tag{21}$$

Now we can use HBM to analyze the transmissibly at large base excitation amplitude as well as the emergence of drift (DC) component in the dynamic response. Substituting the assumed solution in equation (17) into equation (21) produces the following algebraic equations:

$$\begin{cases} \alpha_2\left(U_0{}^2 + \frac{1}{2}(U_1{}^2 + U_2{}^2)\right) + \alpha_3\left(U_0{}^3 + \frac{3}{2}U_0{}^2U_1{}^2 + \frac{3}{2}U_0{}^2U_2{}^2\right) = 0, \\ -\Omega^2 U_1 + 2\Omega\zeta U_2 + 2\alpha_2 U_0 U_1 + \alpha_3\left(3U_0{}^2U_1 + \frac{3}{4}U_1{}^3 + \frac{3}{4}U_1U_2{}^2\right) = \Omega^2 Y, \\ -\Omega^2 U_2 - 2\Omega\zeta U_1 + 2\alpha_2 U_0 U_2 + \alpha_3\left(3U_0{}^2U_2 + \frac{3}{4}U_2{}^3 + \frac{3}{4}U_1{}^2U_2\right) = 0. \end{cases} \tag{22}$$

We Introduce two new variables, A_1 and θ, so that:

$$\begin{cases} U_1 = A_1 \cos\theta, \\ U_2 = -A_1 \sin\theta. \end{cases} \tag{23}$$

The relative displacement (u) can be expressed in terms of the new variables as:

$$u = U_0 + A_1 \cos(\Omega t + \theta), \tag{24}$$

where U_0 represent the drift or DC component of the overall dynamic response, and A_1 represents the primary harmonics or AC component. Through some mathematical manipulations, it can be shown that U_0 satisfies the following ninth-order polynomial equation:

$$\begin{aligned} &\left(-\frac{225}{16}\alpha_3{}^5\right)U_0{}^9 + \left(-\frac{675}{16}\alpha_2\alpha_3{}^4\right)U_0{}^8 \\ &+\left(\frac{45}{4}\Omega^2\alpha_3{}^4 - \frac{795}{16}\alpha_2{}^2\alpha_3{}^3\right)U_0{}^7 \\ &+\left(-\frac{456}{16}\alpha_2{}^3\alpha_3{}^2 + \frac{105}{4}\alpha_2\alpha_3{}^3\Omega^2\right)U_0{}^6 \\ &+\left(-\frac{17}{2}\alpha_2{}^4\alpha_3 + \frac{87}{4}\alpha_2{}^2\alpha_3{}^2\Omega^2\right. \\ &\left.-\frac{9}{4}\alpha_3{}^3\Omega^4 - 9\alpha_3{}^3\zeta^2\Omega^2\right)U_0{}^5 \\ &+\left(-\alpha_2{}^5 + \frac{31}{4}\alpha_2{}^3\alpha_3\Omega^2 - \frac{15}{4}\alpha_2\alpha_3{}^2\Omega^4\right. \\ &\left.-15\alpha_2\alpha_3{}^2\zeta^2\Omega^2\right)U_0{}^4 + \left(\alpha_2{}^4\Omega^2 - \frac{7}{4}\alpha_2{}^2\alpha_3\Omega^4\right. \\ &\left.-7\alpha_2{}^2\alpha_3\zeta^2\Omega^2 - \frac{27}{8}\alpha_3{}^3\Omega^4Y^2\right)U_0{}^3 \\ &+\left(-\alpha_2{}^3\zeta^2\Omega^2 - \frac{1}{4}\alpha_2{}^3\Omega^4 - \frac{27}{8}\alpha_2\alpha_3{}^2\Omega^4Y^2\right)U_0{}^2 \\ &+\left(-\frac{9}{8}\alpha_2{}^2\alpha_3\Omega^4Y^2\right)U_0 - \frac{1}{8}\alpha_2{}^3\Omega^4Y^2 = 0, \end{aligned} \tag{25}$$

which has a non-trivial real solution, indicating the emergence of drift due to the asymmetry in force–displacement curves. Figures 11(a), (b) show the system time responses based on numerical simulation and HBM for $Y = 0.25Na$ and $\Omega = 0.1$ Hz. HBM based on the asymmetric polynomial fitting successfully predicts the drift (DC component) as well as the primary harmonics (AC component).

Moreover, it can also be shown that the following relation holds between U_0 and A_1:

$$A_1{}^2 = -\frac{\alpha_2 U_0{}^2 + \alpha_3 U_0{}^3}{\frac{1}{2}\alpha_2 + \frac{3}{2}\alpha_3 U_0}. \tag{26}$$

And θ can be derived by solving the following equation:

$$\tan\theta = -\frac{2\Omega\zeta}{-\Omega^2 + 2\alpha_2 U_0 + 3\alpha_3 U_0{}^2 + \frac{3}{4}\alpha_3 A_1{}^2}. \tag{27}$$

Once U_0, A_1 and θ are solved, they can be substituted in equation (24) to approximate the steady-state response. We can then use this approximation to calculate the transmissibility (TR) index. Figure 11(c) shows the TR results derived by numerical simulation based on equation (10) and HBM based on asymmetric fitting, respectively. Both results clearly show a significant increase of TR at higher base excitation amplitude. The discrepancy shown in this figure is a result of fitting error from using a relatively low order polynomials. However as mentioned earlier, the purpose of this approximation using HBM is to qualitatively elucidate the effect of asymmetry in force–displacement curves, thus the presented result indeed provides valuable insights into the dynamic behaviors of fluidic origami.

4.3. Base excitation performance analysis

Now that we have an understanding on the influence of asymmetry from the force–displacement relationship, in this section, we comprehensively evaluate the base excitation isolation performance of the fluidic origami based on the actual force–displacement curve. Figure 12(a) represents the correlations among the TR, normalized base excitation amplitude, and excitation frequency. Different colors in this figure represent the value of TR index, and the fluidic origami is considered successful in performing its task when TR < 1. The TR index is consistently below one except at very small frequencies and high base excitation amplitudes (highlighted

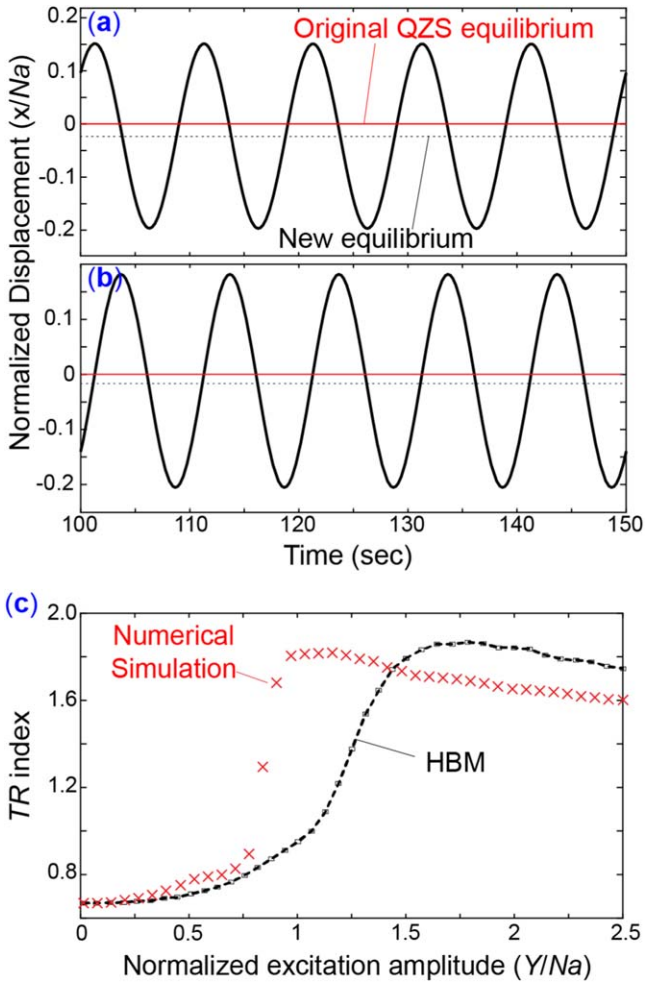

Figure 11. Sample steady-state time responses of system based on (a) numerical simulation and (b) HBM for $Y = 0.25Na$ and $\Omega = 0.1$ Hz. (c) The TR results derived by numerical simulation based on equation (10) and HBM based on asymmetric fitting. Comparing this result to that in figure 7(c), it is evident that the asymmetry plays a crucial role in the high TR values at high excitation amplitude.

region in this figure), therefore, fluidic origami with QZS is indeed an effective isolator.

We further analyze the contribution of drift (DC component) and primary harmonics (AC component) to the overall dynamic response. To this end, FFT analysis is applied to the steady-state time responses corresponding to different excitation frequencies and amplitudes. Figures 12(b), (c) show the magnitudes of DC (DC/Y) and AC (AC/Y) components, respectively.

It can be seen that at some regions of base excitation frequency and amplitude, the TR index is high and dominated by the AC component. Figure 12(d) shows such an example where $Y/Na = 1.4$ and $\Omega = 0.1$ Hz. In contrary, there are some combinations of excitation frequencies and amplitudes by which the DC components dominates, and an example corresponding to $Y/Na = 0.8$ and $\Omega = 1$Hz is shown in figure 12(e). The significant drift in the time response can drive the TR index to near one. Therefore, unlike other QZS vibration isolators with symmetric force–displacement relationships, drift plays a considerable role in the system dynamics. One needs to consider its effect carefully in order to properly explain the base excitation isolation.

Another important factor that needs to be considered is the limit of achievable displacement of the fluidic origami. The length of fluidic origami is restricted by the kinematics of folding, that is, the structure can only be stretched up to the fully deployed state ($\theta_I = 0^\circ$ shown in figure 2(b)). Therefore, we have to ensure that the maximum relative displacement $u(t)$ of the end mass does not exceed the maximum length of fluidic origami.

As the first step to understand the effect of such a geometric constraint due to folding, we show that the maximum allowed displacement from the QZS configuration to the fully deployed configuration is linearly related to the number of unit cells in a fluidic origami tubular channel. It can be shown that the folding angle at the QZS configuration (θ_{QZS}) does not depend on the number of cells. Therefore, from equation (1) we can write the maximum possible displacement from QZS to the fully deployed state as:

$$\Delta x = N\left(\frac{2b\tan\gamma_I}{\sqrt{1+\tan\gamma_I^2}} - \frac{2b\cos\theta_{QZS}\tan\gamma_I}{\sqrt{1+\cos\theta_{QZS}^2\tan\gamma_I^2}}\right), \quad (28)$$

Based on equation (28), the relationship between the maximum possible displacement (Δx) and the number of cells (N) is linear (figure 13(a)). This result can then be applied to the parametric analysis result shown in figure 12(a) as a constraint. That is, if the maximum end mass displacement is larger than Δx at some frequencies and base excitation magnitudes, the fluidic origami is no longer considered feasible for vibration isolation. Figure 13(b) shows such a region where the end mass displacement exceed the constraint of folding. We can see that based excitation frequency and amplitude combinations that leads to TR > 1 is indeed unachievable. In another words, as long as the fluidic origami is not stretched to its maximum length, it can always perform well as a low-frequency base excitation isolator. Moreover, fluidic origami with more unit cells in its tubular channel can isolate base excitation with larger amplitudes.

5. Summary and conclusion

This study analytically and experimentally examines a pressurized origami cellular structure with an asymmetric QZS property, and investigates its use in low-frequency vibration isolation. Fluidic origami consisting of SMO sheets has been shown to exhibit many unique and interesting mechanical properties related to stiffness. This research demonstrates that by sealing the pressurized structure, it is possible to acquire QZS property due to the intricate and nonlinear relationship between folding and internal volume change. Design guidelines for achieving QZS are presented for two different cases: One is ISMO and the other is NISMO. A proof-of-concept prototype was tested to verify the existence of desired QZS property. The appropriate fluidic origami designs are then used for a comprehensive dynamic study of low-frequency

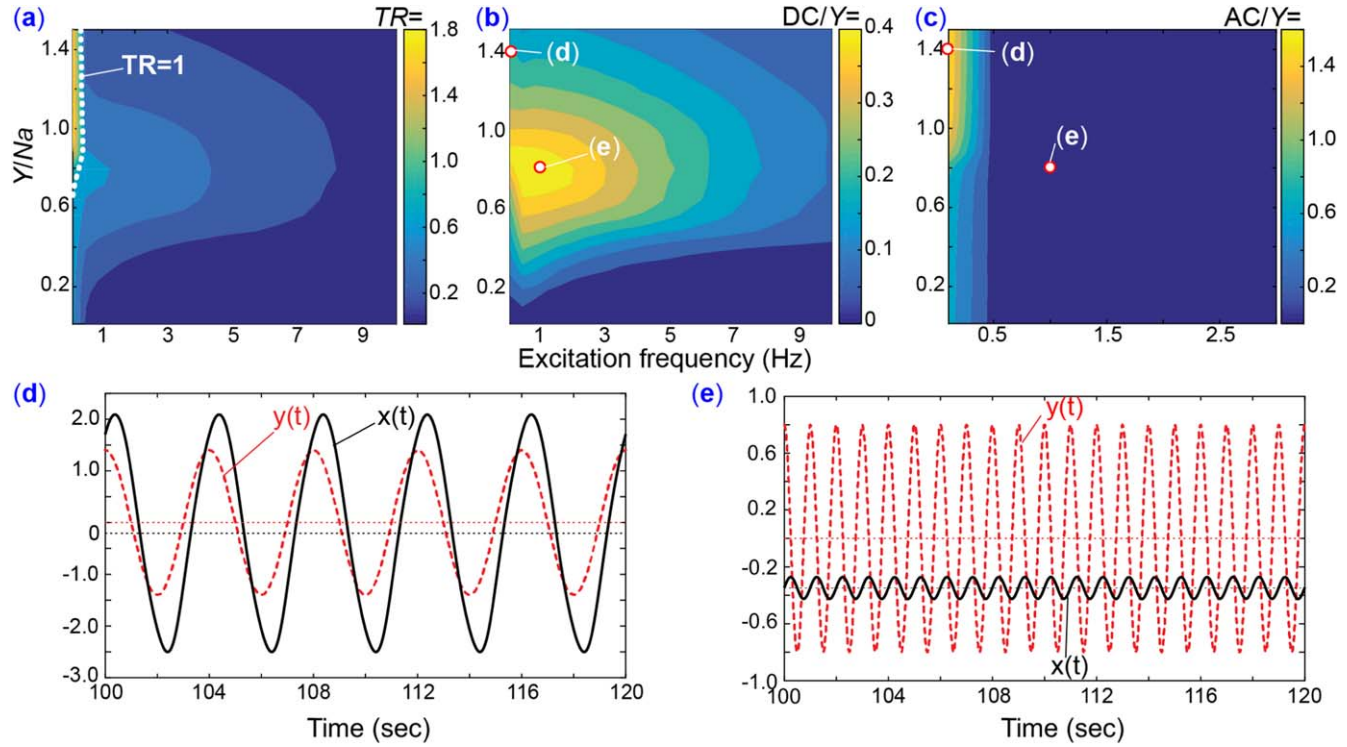

Figure 12. Base excitation performance study (a) The relationship among the TR index magnitude, normalized excitation amplitude and normalized excitation frequency. The performance threshold of TR = 1 is highlighted. (b) and (c) show the corresponding contribution of DC and AC components in the response, respectively. (d) Sample time-response at $Y/Na = 1.4$ and $\Omega = 0.1$ Hz, showing an AC dominated response of AC term. (e) Another Sample time-response at $Y/Na = 0.8$ and $\Omega = 1$ Hz, showing a DC dominated response.

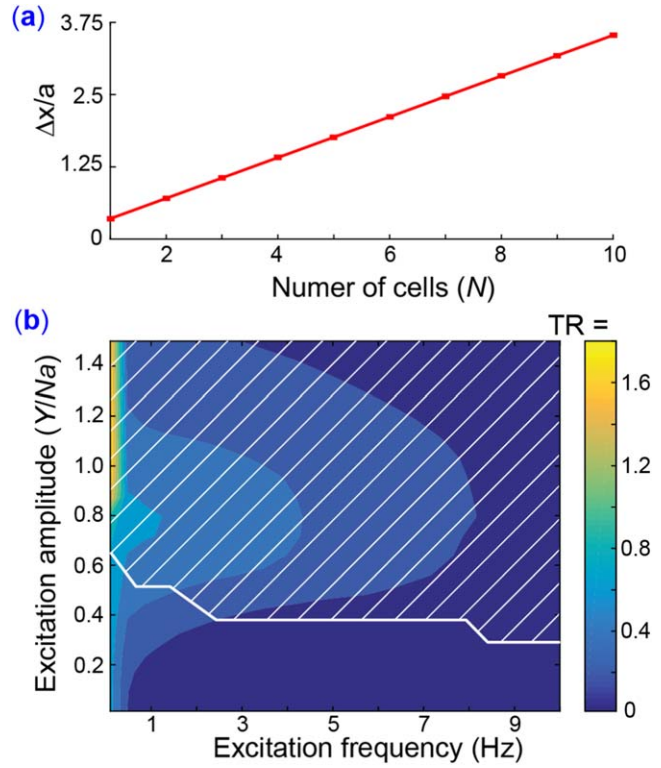

Figure 13. (a) The linear relation between the maximum possible displacement (Δx) and the number of cells (N). (b) The shaded regions show the excitation magnitudes and frequencies at which maximum relative displacement of the end mass exceeds the folding limitation of the fluidic origami.

base-excitation isolation. In particular, this study closely examines the effects of inherent asymmetry in the force–displacement relationships of fluidic origami. Via comparing the approximation solutions based on HBM using both symmetric and asymmetric polynomial fittings, we show that the asymmetry in force–displacement curve can (1) induce a significant drift (DC component) in the steady state time response and (2) increase the TR at high excitation amplitude and low frequency. These phenomena must be carefully considered for evaluating the base excitation isolation performance. Moreover, the kinematic constraint due to folding is also considered to ensure that fluidic origami will not be stretched beyond its maximum possible length. We show that QZS property from fluidic origami can indeed provide effective base excitation isolation at low-frequencies. The internal pressure of fluidic origami can be adjusted to accommodate changes in the end mass, making the cellular structure tunable. Results of this study can lay the foundation of origami-inspired metamaterials and meta-structures with embedded dynamic functionalities. Moreover, investigations into the asymmetry in force–displacement relationship provide valuable insights for many other QZS structures with similar properties.

Acknowledgments

S Sadeghi and S Li acknowledge the support from National Science Foundation (Award # CMMI-1634545,

CMMI-1751449 CAREER, and CMMI-1760943) and the Clemson University (via startup funding and Dean's Faculty Fellow Award).

ORCID iDs

Sahand Sadeghi https://orcid.org/0000-0003-2657-4953
Suyi Li https://orcid.org/0000-0002-0355-1655

References

Abbasi A *et al* 2016 Vibration control of a rotor supported by journal bearings and an asymmetric high-static low-dynamic stiffness suspension *Nonlinear Dyn.* **85** 525–45
Abolfathi Ali 2012 Nonlinear vibration isolators with asymmetric stiffness *PhD Thesis* University of Southampton (https://eprints.soton.ac.uk/355884)
Alabuzhev P M *et al* 1989 *Vibration Protecting and Measuring Systems with Quasi-Zero Stiffness* (New York: CRC Press)
Andersen E S *et al* 2009 Self-assembly of a nanoscale DNA box with a controllable lid *Nature* **459** 73–6
Carrella A 2008 Passive vibration isolators with high-static-low-dynamic-stiffness *PhD Thesis* University of Southampton (https://eprints.soton.ac.uk/51276)
Carrella A, Brennan M J and Waters T P 2007 Static analysis of a passive vibration isolator with quasi-zero-stiffness characteristic *J. Sound Vib.* **301** 678–89
Carrella A *et al* 2009a On the force transmissibility of a vibration isolator with quasi-zero-stiffness *J. Sound Vib.* **322** 707–17
Carrella A *et al* 2009b Using nonlinear springs to reduce the whirling of a rotating shaft *Mech. Syst. Sig. Process.* **23** 2228–35
Carrella A *et al* 2012 Force and displacement transmissibility of a nonlinear isolator with high-static-low-dynamic-stiffness *Int. J. Mech. Sci.* **55** 22–9
Cheung K C *et al* 2014 Origami interleaved tube cellular materials *Smart Mater. Struct.* **23** 094012
Daynes S, Trask R S and Weaver P M 2014 Bio-inspired structural bistability employing elastomeric origami for morphing applications *Smart Mater. Struct.* **23** 125011
Dietz H, Douglas S M and Shih W M 2009 Folding DNA into twisted and curved nanoscale shapes *Science* **325** 725–30
Eidini M 2016 Zigzag-base folded sheet cellular mechanical metamaterials *Extreme Mech. Lett.* **6** 96–102
Eidini M and Paulino G H 2015 Unravelling metamaterial properties in zigzag-base folded *Sci. Adv.* **1** e1500224
Fang H, Li S and Wang K W 2016 Self-locking degree-4 vertex origami structures *Proc. R. Soc.* A **472** 20160682
Fang H *et al* 2016 Uncovering the deformation mechanisms of origami metamaterials by introducing generic degree-four vertices *Phys. Rev.* E **94** 043002
Fang H, Wang K W and Li S 2017 Asymmetric energy barrier and mechanical diode effect from folding multi-stable stacked-origami *Extreme Mech. Lett.* **17** 7–14
Fang H *et al* 2017 Dynamics of a bistable Miura-origami structure *Phys. Rev.* E **95** 052211
Felton S *et al* 2014 A method for building self-folding machines *Science* **345** 644–6
Filipov E T, Tachi T and Paulino G H 2015 Origami tubes assembled into stiff, yet reconfigurable structures and metamaterials *Proc. Natl Acad. Sci.* **112** 12321–6
Fulcher B A *et al* 2014 Analytical and experimental investigation of buckled beams as negative stiffness elements for passive vibration and shock isolation systems *J. Vib. Acoust.* **136** 031009
Gramüller B, Boblenz J and Hühne C 2014 PACS—realization of an adaptive concept using pressure actuated cellular structures *Smart Mater. Struct.* **23** 115006
Hamdan M N and Burton T D 1993 On the steady state response and stability of non-linear oscillators using harmonic balance *J. Sound Vib.* **166** (2) 255–66
Hanna B H *et al* 2014 Waterbomb base: a symmetric single-vertex bistable origami mechanism *Smart Mater. Struct.* **23** 094009
Hao Z and Cao Q 2015 The isolation characteristics of an archetypal dynamical model with stable-quasi-zero-stiffness *J. Sound Vib.* **340** 61–79
Harrington M J *et al* 2011 Origami-like unfolding of hydro-actuated ice plant seed capsules *Nat. Commun.* **2** 337
Huang X C, Liu X T and Hua H X 2014 Effects of stiffness and load imperfection on the isolation performance of a high-static-low-dynamic-stiffness non-linear isolator under base displacement excitation *Int. J. Non-Linear Mech.* **65** 32–43
Inamoto K and Ishida S 2018 Improved feasible load range and its effect on the frequency response of origami-inspired vibration isolators with quasi-zero-stiffness characteristics *J. Vib. Acoust.* **141** 021004
Ishida S, Suzuki K and Shimosaka H 2017a Design and experimental analysis of origami-inspired vibration isolator with quasi-zero-stiffness characteristic *J. Vib. Acoust.* **139** 051004
Ishida S *et al* 2017b Design and numerical analysis of vibration isolators with quasi-zero-stiffness characteristics using bistable foldable structures *J. Vib. Acoust.* **139** 031015
Kaino K, Yajima K and Chiba N 2000 Origami modeling method of leaves of plants and CG image generation of flower arrangement *Proceedings Seventh International Conference on Parallel and Distributed Systems: Workshops* 207–12
Kamrava S *et al* 2017 Origami-based cellular metamaterial with auxetic, bistable, and self-locking properties *Sci. Rep.* **7** 46046
Ke Y *et al* 2009 Scaffolded DNA origami of a DNA tetrahedron molecular container *Nano Lett.* **9** 2445–7
Kovacic I, Brennan M J and Lineton B 2009 Effect of a static force on the dynamic behaviour of a harmonically excited quasi-zero stiffness system *J. Sound Vib.* **325** 870–83
Kovacic I, Brennan M J and Waters T P 2008 A study of a nonlinear vibration isolator with a quasi-zero stiffness characteristic *J. Sound Vib.* **315** 700–11
Kuribayashi K *et al* 2006 Self-deployable origami stent grafts as a biomedical application of Ni-rich TiNi shape memory alloy foil *Mater. Sci. Eng.* A **419** 131–7
Lee C M, Goverdovskiy V N and Temnikov A I 2007 Design of springs with 'negative' stiffness to improve vehicle driver vibration isolation *J. Sound Vib.* **302** 865–74
Li S, Fang H and Wang K W 2016 Recoverable and programmable collapse from folding pressurized origami cellular solids *Phys. Rev. Lett.* **117** 1–5
Li S and Wang K W 2015 Fluidic origami: a plant-inspired adaptive structure with shape morphing and stiffness tuning *Smart Mater. Struct.* **24** 105031
Li S *et al* 2019 Architected Origami Materials: How Folding Creates Sophisticated Mechanical Properties *Adv. Mater.* **31** 1805282
Miura K 1985 Method of packaging and deployment of large membranes in space *The Institute of Space and Astronautical Science Report* **618** 1–9 (https://repository.exst.jaxa.jp/dspace/handle/a-is/7293)
Na J H *et al* 2015 Programming reversibly self-folding origami with micropatterned photo-crosslinkable polymer trilayers *Adv. Mater.* **27** 79–85
Nayfeh A H 1993 *Introduction to Perturbation Techniques* (New York: Wiley)
Neild S A and Wagg D J 2011 Applying the method of normal forms to second-order nonlinear vibration problems *Proc. R. Soc.* **467** 1141–63

Peraza-Hernandez E A *et al* 2014 Origami-inspired active structures: a synthesis and review *Smart Mater. Struct.* **23** 094001

Sadeghi S and Li S 2017 Harnessing the quasi-zero stiffness from fluidic origami for low frequency vibration isolation *ASME 2017 Conference on Smart Materials, Adaptive Structures and Intelligent Systems Volume 2: Modeling, Simulation and Control of Adaptive Systems; Integrated System Design and Implementation; Structural Health Monitoring* 18 (ASME) pp V002T03A008 (https://doi.org/10.1115/SMASIS2017-3754)

Sadeghi Sahand and Li Suyi 2019 Analyzing the bi-directional dynamic morphing of a bi-stable water-bomb base origami *Proc. SPIE* **10968** 109680S

Schenk M and Guest S D 2013 Geometry of Miura-folded metamaterials *Proc. Natl Acad. Sci.* **110** 3276–81

Schenk M *et al* 2014 Review of inflatable booms for deployable space structures: packing and rigidization *J. Spacecr. Rockets* **51** 762–78

Sengupta S and Li S 2018 Harnessing the anisotropic multi-stability of stacked-origami mechanical metamaterials for elastic modulus programming *J. Intel. Mater. Syst. Struct.* **29** 2933–45

Shaw A D, Neild S A and Wagg D J 2013 Dynamic analysis of high static low dynamic stiffness vibration isolation mounts *J. Sound Vib.* **332** 1437–55

Shih W M and Lin C 2010 Knitting complex weaves with DNA origami *Curr. Opin. Struct. Biol.* **20** 276–82

Silverberg J L *et al* 2015 Origami structures with a critical transition to bistability arising from hidden degrees of freedom *Nat. Mater.* **14** 389–93

Song Z *et al* 2014 Origami lithium-ion batteries *Nat. Commun.* **5** 3140

Street T 2002 Deployable membranes designed *Phil. Trans. R. Soc. A* **360** 227–38

Tachi T 2010a Freeform rigid-foldable structure using bidirectionally flat-foldable planar quadrilateral mesh *Advances in Architectural Geometry* ed C Ceccato *et al* (Vienna, Austria: Springer) pp 87–102

Tachi T 2010b Origamizing polyhedral surfaces *IEEE Trans. Vis. Comput. Graphics* **16** 298–311

Tachi T 2011 Rigid foldable thick origami *Origami 5* ed P Wang-Iverson *et al* vol 5 1st edn (Boca Raton, FL: A K Peters/CRC Press) pp 253–64

Thomson W 1996 *Theory of Vibration With Applications* 1st edn (Boca Raton, FL: CRC Press) 9780748743803

Waitukaitis S and van Hecke M 2016 Origami building blocks: Generic and special four-vertices *Phys. Rev.* E **93** 023003

Yasuda H and Yang J 2015 Reentrant origami-based metamaterials with negative Poisson's ratio and bistability *Phys. Rev. Lett.* **114** 185502

Yasuda H *et al* 2016 Formation of rarefaction waves in origami-based metamaterials *Phys. Rev.* E **93** 043004

Yoshimura Y 1951 On the mechanism of buckling of a circular cylindrical shell under axial compression *The Reports of the Institute of Science and Technology University of Tokyo NACA-TM-1390* National Advisory Committee for Aeronautics; Washington, DC, United States (https://ntrs.nasa.gov/search.jsp?R=19930093840)

Zhou J *et al* 2015 Nonlinear dynamic characteristics of a quasi-zero stiffness vibration isolator with cam-roller-spring mechanisms *J. Sound Vib.* **346** 53–69

Fang Hongbin, Chu Shih-Cheng A. and Wang Kon-Well 2018 Programmable Self-Locking Origami Mechanical Metamaterials *Adv. Mater.* **30** 1706311

Zhou N and Liu K Ã 2010 A tunable high-static—low-dynamic stiffness vibration isolator *J. Sound Vib.* **329** (9) 1254–73

Zirbel S A *et al* 2013 Accommodating thickness in origami-based deployable arrays *J. Mech. Des.* **135** 111005